

Optical Imaging of Anatomical Maps Derived from Magnetic Resonance Images Using Time-Independent Optical Sources

Jenghwa Chang, *Member, IEEE*, Harry L. Graber, *Student Member, IEEE*, Ping Chen Koo, Raphael Aronson, San-Lian S. Barbour, *Member, IEEE*, and Randall L. Barbour,* *Member, IEEE*

Abstract—We present a model suitable for computing images of absorption cross sections of thick tissue structures illuminated at near infrared (NIR) wavelengths from tomographic projection data. Image reconstruction is accomplished by solving a system of linear equations derived from transport theory. Reconstruction results using different algebraic solvers are shown for anatomical maps of the breast, derived from magnetic resonance imaging data, containing two simulated pathologies, in which case qualitatively good reconstructions were obtained. Evaluation of magnetic resonance (MR) data to optimize NIR optical tomographic imaging methods and to assess the feasibility of a combined MR-optical measurement scheme is discussed.

Index Terms—Dense scattering medium, inverse problem, optical tomography.

I. INTRODUCTION

IT is known that light of wavelengths between 700 and 1300 nm can penetrate deeply into tissue [1]. Through this window it is possible to monitor, for example, clinically important conditions associated with oxygen-deficient states [2]. The extension of this capability to an imaging mode is an objective that has been sought for many years. In contrast to other, more established, imaging methods [e.g., X-ray computed tomography (CT), positron emission tomography (PET), or single photon emission computed tomography (SPECT)], the principal obstacle to imaging at near infrared (NIR) wavelengths is the overwhelming amount of scattering of the penetrating photons. The mean free pathlength (mfp) for scattering is typically on the order of 100 μm , and the scattering cross section is at least two orders of magnitude greater than that for absorption [1]. A consequence of this is

that the projection-slice theorem of X-ray CT is not directly applicable.

To make direct use of the scattered signal, many groups [3]–[8], including ourselves [7], [8], have described solutions to the inverse problem using perturbation methods. These require specification of a reference medium and produce an image that is related to the difference between the optical cross sections of the target and reference media. The equations that must be inverted are linear, but to obtain an accurate image it may be necessary to solve many linear systems in sequence, while recomputing the imaging operator (i.e., the coefficients in the linear equations) after each inverse calculation. In general, the greater the difference between the media, the larger the number of iterations needed before the solution converges. This strategy is similar to, for example, techniques used by Chew and coworkers for microwave imaging, such as their Born iterative [9] and distorted Born iterative [10] methods.

A clinical problem of interest to many groups is the application of optical techniques as a complement to X-ray mammography. This interest has been stimulated by a growing concern over the large and increasing percentage of women who will develop breast cancer, published reports of low positive and negative predictive powers by mammography [11], and growing concern over the possible baneful effects of the X-rays employed [11]. Because of alterations in cell chemistry and local blood supply, transformed cells frequently exhibit derangements in cell shape, internal organelle composition, and cellular function that can be associated with abnormal ratios of the various chemical or electronic states of heme proteins [12]. It is hoped that the sensitivity of light absorption to changes in these ratios, and/or of scattering to the cell shape or organelle changes, will ultimately allow one to detect nascent tumors in the breast before they have developed any anatomical peculiarities that would cause them to be detectable mammographically. Additional advantages of optical methods are they are nonionizing and potentially employ low-cost instrumentation.

The objective of this study is to introduce the idea of evaluating magnetic resonance (MR) data in order to construct anatomically accurate optical (AAO) models of tissue. This is analogous to the use of priors obtained from X-ray CT or MR images to assist in the reconstruction of functional PET or SPECT images, as has been described previously

Manuscript received December 13, 1994; revised October 8, 1996. This work was supported in part by the National Institutes of Health (NIH) under Grant ROI-CA59955 and the New York State Science and Technology Foundation. The Associate Editor responsible for coordinating the review of this paper and recommending its publication was M. W. Vannier. *Asterisk indicates corresponding author.*

J. Chang is with the Department of Pathology, SUNY Health Science Center at Brooklyn, Brooklyn, NY 11203 USA.

H. L. Graber is with the Program in Physiology and Biophysics, SUNY Health Science Center at Brooklyn, Brooklyn, NY 10023 USA.

P. C. Koo, R. Aronson, and S.-L. S. Barbour are with the Bioimaging Sciences Corporation, West Orange, NJ 07052 USA.

*R. L. Barbour is with the Department of Pathology and the Program in Physiology and Biophysics, SUNY Health Science Center at Brooklyn, 450 Clarkson Avenue, Brooklyn, NY 11203 USA (e-mail: barbour@sacc.hscbklyn.edu).

Publisher Item Identifier S 0278-0062(97)00985-3.

by, for example, Gindi *et al.* [13] and by Leahy and Yan [14]. In this study, we have elected to use MR data because of its excellent contrast among soft tissue types and the fact that, in practice, three-dimensional (3-D) information is often readily available. We have also sought to evaluate MR-derived phantoms because we believe that this represents an efficient means of optimizing data collection and analysis schemes using a model for which the size, location, number, and contrast of added inclusions can be easily varied within an anatomically accurate background. Our goal has been to employ the AAO models both as a means for optimizing algorithm development and data collection, and also to assess the feasibility of integrating the MR and optical methods. Preliminary descriptions of these findings have been presented elsewhere [15], [16]. A derivation of the modeling scheme used for imaging in highly scattering media is described below.

II. PERTURBATION MODEL

The migration of monoenergetic photons through an isotropic medium can be described by the time-independent transport equation [17]

$$\Omega \cdot \nabla \phi + \mu_T \phi - \int_{4\pi} \mu_s(\Omega' \cdot \Omega) \phi d\Omega' = q \quad (1)$$

where $d\Omega$ = differential solid angle about the direction Ω of a spherical polar coordinate system; ϕ = angular intensity at \mathbf{r} in direction Ω [photons/area/solid angle /time]; q = angular source density at \mathbf{r} in direction Ω [photons/volume/solid angle/time]; $\mu_s(\Omega' \cdot \Omega)$ = macroscopic differential scattering cross section at \mathbf{r} from direction Ω' into direction Ω [1/length/solid angle]; and μ_T = macroscopic total cross section at \mathbf{r} [1/length]. In addition, $\mu_T = \mu_a + \mu_s$, where μ_a is the macroscopic absorption cross section at \mathbf{r} [1/length] and $\mu_s = \int_{4\pi} \mu_s(\Omega \cdot \Omega') d\Omega'$ is the macroscopic scattering cross section at \mathbf{r} [1/length].

Let the angular intensity and absorption cross section be perturbed, $\phi \rightarrow \phi + \Delta\phi$ and $\mu_a \rightarrow \mu_a + \Delta\mu_a$. We substitute the perturbed quantities into (1), subtract the original (1) from the result, and assume the perturbations are small enough that the second-order terms (i.e., those proportional to $\Delta\mu_a \Delta\phi$) can be ignored. Then the transport equation for the angular intensity *perturbation* becomes

$$\Omega \cdot \nabla(\Delta\phi) + \mu_T \Delta\phi - \int_{4\pi} \mu_s(\Omega' \cdot \Omega) \Delta\phi d\Omega' = -\Delta\mu_a \phi. \quad (2)$$

That is, if ϕ is the solution satisfying the boundary conditions with a source q , then $\Delta\phi$ is the solution satisfying the same boundary conditions with the equivalent source $q_e = -\Delta\mu_a \phi$. Let $G(\mathbf{r}_1, \Omega_1; \mathbf{r}_2, \Omega_2)$ be the Green's function satisfying (1) at \mathbf{r}_1 in direction Ω_1 under a given set of boundary conditions, with a unit-strength source at \mathbf{r}_2 in direction Ω_2 . Assume further that the form of the source function is $q = \delta(\mathbf{r} - \mathbf{r}_q) \delta(\Omega - \Omega_q)$ and that the detector response function, r , is $r = r(\mathbf{r}_d, \Omega_d) \delta(\mathbf{r} - \mathbf{r}_d) \delta(\Omega - \Omega_d)$ (i.e., we are using a perfectly collimated point detector), and apply a well-known reciprocity theorem, $G(\mathbf{r}_1, \Omega_1; \mathbf{r}_2, \Omega_2) =$

$G(\mathbf{r}_2, -\Omega_2; \mathbf{r}_1, -\Omega_1)$ [18]. Then the change in detector reading due to the perturbation is

$$\Delta R = - \int_V \Delta\mu_a \int_{4\pi} G(\mathbf{r}, \Omega; \mathbf{r}_q, \Omega_q) G(\mathbf{r}, -\Omega; \mathbf{r}_d, -\Omega_d) d\Omega d^3r. \quad (3)$$

If we expand the Green's functions in spherical harmonics and assume that only the constant and linear terms of the expansions are significant [19], we obtain

$$\begin{aligned} G(\mathbf{r}, \Omega; \mathbf{r}_q, \Omega_q) &\cong \frac{1}{4\pi} (\phi_0 + 3\mathbf{J}_0 \cdot \Omega) \\ G(\mathbf{r}, -\Omega; \mathbf{r}_d, -\Omega_d) &\cong \frac{1}{4\pi} (\phi_0^+ + 3\mathbf{J}_0^+ \cdot \Omega) \end{aligned} \quad (4)$$

where $\phi_0 = \int_{4\pi} G(\mathbf{r}, \Omega; \mathbf{r}_q, \Omega_q) d\Omega$, $\mathbf{J}_0 = \int_{4\pi} G(\mathbf{r}, \Omega; \mathbf{r}_q, \Omega_q) \Omega d\Omega$, $\phi_0^+ = \int_{4\pi} G(\mathbf{r}, \Omega; \mathbf{r}_d, \Omega_d) d\Omega$, and $\mathbf{J}_0^+ = - \int_{4\pi} G(\mathbf{r}, -\Omega; \mathbf{r}_d, -\Omega_d) \Omega d\Omega$ are the direct and adjoint intensities (ϕ_0, ϕ_0^+) and fluxes ($\mathbf{J}_0, \mathbf{J}_0^+$), respectively. Then (3) becomes

$$\Delta R = \int_V w_a \Delta\mu_a d^3r \quad (5)$$

where

$$w_a = \frac{-(\phi_0 \phi_0^+ - 3\mathbf{J}_0 \cdot \mathbf{J}_0^+)}{4\pi} \quad (6)$$

is the weight function. (This derivation was made strictly in terms of perturbations in μ_a because this was the only cross section perturbed in the specific examples presented in this report. We have made the analogous derivation of the formula for the weight function corresponding to perturbations in μ_s , but do not show it here.)

If the scattering is anisotropic, as is the case in most biological tissues, it is appropriate to use the *reduced* scattering cross section, μ'_s , and *transport* cross section, μ_{tr} , in place of, respectively, μ_s and μ_T . The operational definitions of these quantities are $\mu'_s = (1 - f_1) \mu_s$, where $f_1 = \int_{4\pi} \mu_s(\Omega' \cdot \Omega) \Omega' \cdot \Omega d\Omega' / \int_{4\pi} \mu_s(\Omega' \cdot \Omega) d\Omega'$ is the first moment of the differential scattering cross section, and $\mu_{tr} = \mu_a + \mu'_s$. This, in conjunction with the preceding approximations, will lead to the diffusion approximation to the transport equation [20]

$$-\nabla \cdot (D \nabla \Phi) + \mu_a \Phi = Q \quad (7)$$

where $\Phi = \int_{4\pi} \phi d\Omega$, $Q = \int_{4\pi} q d\Omega$, $D = 1/3(\mu_a + \mu'_s)$. By solving for Φ in (7), ϕ_0 and ϕ_0^+ in (4) can be readily obtained. The magnitude of the flux is usually much smaller than the intensity, so that the second term in the numerator of (6) can be safely neglected. (There are regions, such as voxels in the immediate vicinity of the external boundary, where the second term is significant and should be retained.) Numerical solvers for the diffusion equation are much faster than Monte Carlo simulations for solving the transport equation and so provide an efficient alternative way to obtain the weight functions in (6). One difficulty encountered when using the diffusion approximation is specification of the correct boundary conditions. This is still an open question, and many groups, including ours, are investigating this. Most groups have adopted an extrapolated boundary condition when using the diffusion approximation to solve transport problems. However, as recently

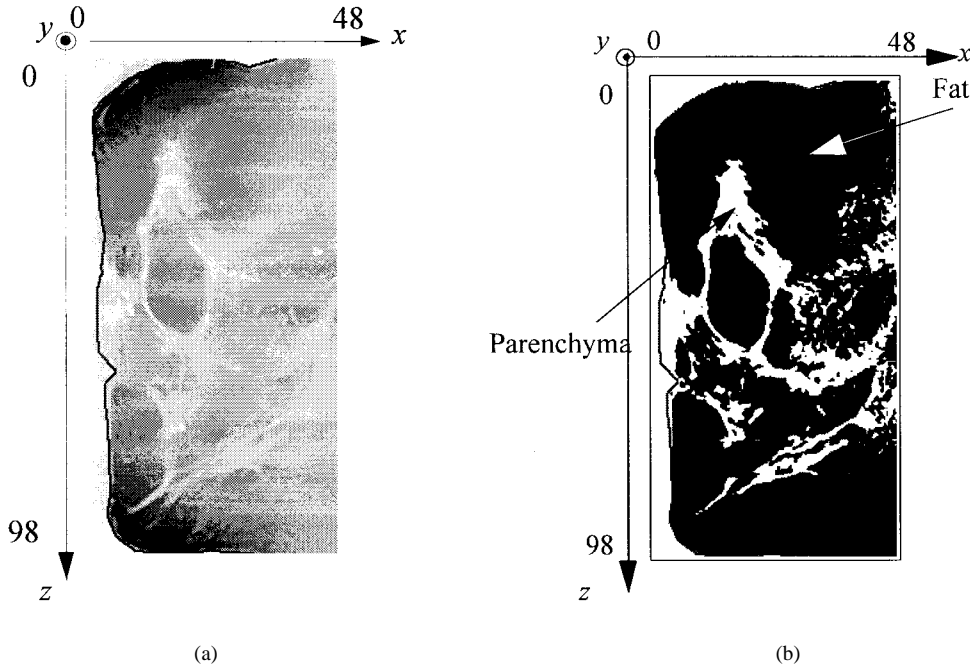


Fig. 1. Illustration of segmentation of one sagittal cut of a MR breast image: (a) original 98×48 MR image and (b) segmented 98×48 MR image. The adipose and parenchymal tissues were segmented using simple thresholding.

pointed out by Aronson [21], the extrapolation distance must be carefully chosen to avoid serious modeling errors.

Equation (5) can also be represented in discretized matrix form. Let the target medium be discretized into J voxels and $\Delta\mu_{a,j}$ be the volume-averaged perturbation of the absorption cross section in voxel j . Let I be the total number of source-detector pairs and ΔR_i be the detector reading for the i th source-detector pair; then (5) can be written as a system of linear equations

$$\Delta \mathbf{R} = \mathbf{W} \Delta \mu \quad (8)$$

where $\Delta \mathbf{R}$ are $\Delta \mu$ vectors for the detector readings and absorption coefficients, and \mathbf{W} is the weight matrix whose elements are the integrated weight function of each voxel.

The inverse problem can be stated as follows: given a set of source-detector pairs, the perturbed detector readings $\Delta \mathbf{R}$, and the precalculated weight function \mathbf{W} , find the perturbation of the macroscopic absorption cross sections $\Delta \mu$ of the target medium.

III. METHODS

A series of sagittal MR breast images was obtained using a General Electric (Milwaukee, WI) Signa MR system. The fast spin echo (TR = 4000 ms, TE = 112 ms, 3-mm thickness) technique was used with and without fat and water saturation. Surface coils were used to obtain better uniformity of the field. Fig. 1(a) shows a sagittal section through one such image. This series of sagittal sections was then used as the reference medium in image reconstructions of the entire 3-D breast volume, a $48 \times 70 \times 98$ array of voxels. Although the whole array of voxels is a rectangular parallelepiped, some of the voxels were not occupied by breast tissue—the region of interest (ROI)—and were treated as free space.

TABLE I

THE CROSS SECTIONS (μ_a AND μ_s) ASSIGNED TO PHANTOMS RECONSTRUCTED FROM MR BREAST IMAGES. PAR. = PARENCHYMA, PATH. = PATHOLOGY. "n.c." MEANS "NO CHANGE," THAT IS, THE CROSS SECTION REMAINS THE SAME AS THAT OF THE ADIPOSE OR PARENCHYMAL TISSUE WITHOUT PATHOLOGY. THE DIMENSIONS OF μ_a AND μ_s ARE mm^{-1}

	Fat	Par.	Path.
μ_a	0.01	0.03	0.05
μ_s	1.00	0.50	n.c.

Each pixel in the digitized MR image was assigned an integer value in the range 0–255. The border between the breast and free space was first extracted using National Institutes of Health (NIH) image software on a Macintosh computer. This divided each image into two regions, the free-space region and the breast region (the ROI). The breast region was then segmented into two different tissue types, "fat" and "parenchyma." The segmentation was accomplished via a simple thresholding technique, in which all MR image pixels possessing image intensities <128 were assigned to be parenchyma tissue and those with image intensities ≥ 128 were assumed to be adipose tissue. Fig. 1(b) shows a sagittal section of a segmented image. We are aware that the image segmentation protocol used here is crude, and have implemented more accurate methods in other studies [22]. Each tissue type was then assigned a set of physical properties— μ_a and μ_s' —as listed in Table I. These optical properties for the complex object (Table I) are sensible, but somewhat arbitrary in that little is known about the optical properties of breast tissue and tumors *in vivo*. For voxels outside the ROI, μ_a and μ_s' are both set to zero for free space. Two pathologies, as shown in Fig. 2, were introduced by assigning the μ_a values listed in Table I. The $6 \times 6 \times 6$ arrays of voxels corresponding to

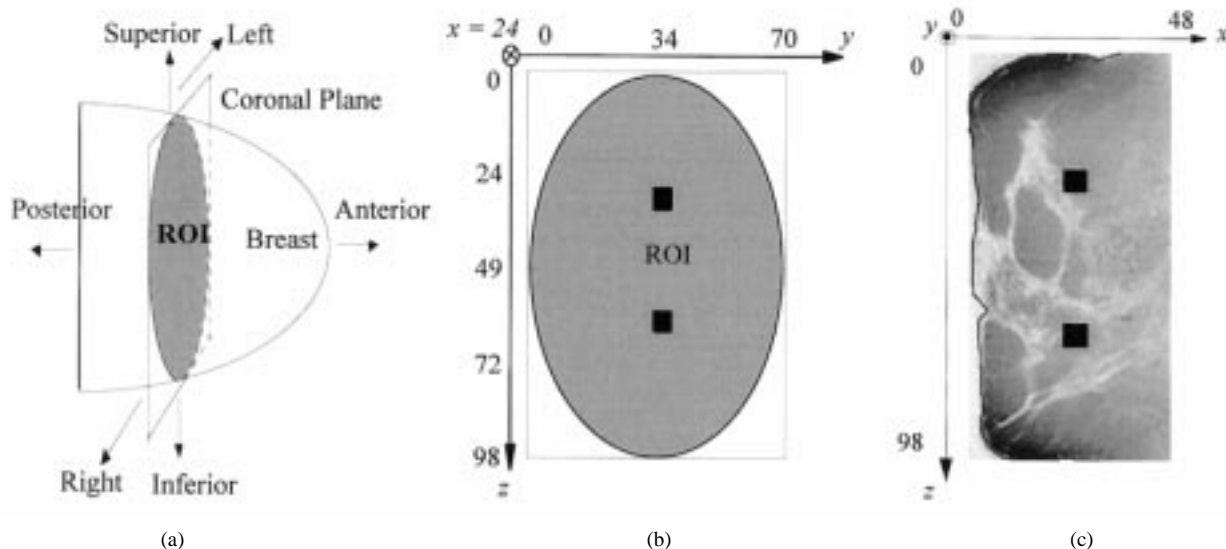


Fig. 2. (a) Illustration of the breast geometry and (b) illustration of a coronal section through a breast phantom, showing the locations of the introduced “pathologies.” Rectangular border indicates the entire discretized volume, shaded elliptical area indicates the ROI, and the black squares are the pathologies. (c) A sagittal view of the AAO model, showing locations of the pathologies.

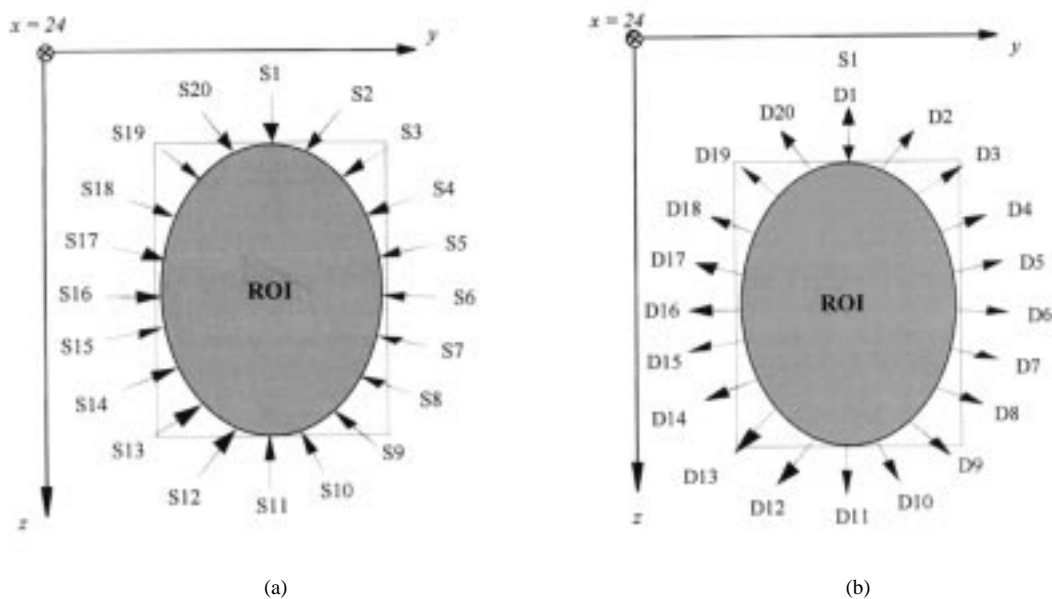


Fig. 3. (a) The 20 source locations modeled for the forward diffusion computations in the MR breast image study and (b) 20 detector locations for source one (S1).

the pathologies were positioned halfway between the chest wall and nipple [Fig. 2(c)] and halfway between the right and left lateral aspects [Fig. 2(b)]. In the third dimension, the pathologies were located one and two thirds of the way from the superior to the inferior margins of the breast. The values chosen for the scattering cross sections are about the same as would be expected in a real breast ($\sim 1 \text{ mm}^{-1}$) [23]. Under this assumption, it is reasonable to use voxels of size $1.35 \times 1.35 \times 1.35 \text{ mm}^3$, which corresponds to a breast having dimensions of $6.5 \times 9.5 \times 13.2 \text{ cm}^3$, or a volume of approximately 730 cm^3 , and pathologies having dimensions of $0.81 \times 0.81 \times 0.81 \text{ cm}^3$, or a volume of approximately 0.53 cm^3 . The schematic shown in Fig. 2(a) and (b) is highly

idealized. The actual geometry of the breast was not elliptical or even bilaterally symmetric.

Solutions to the direct problem for 3-D MR breast data were computed using a relaxation code [24], which is a numerical method used to solve the diffusion equation. An extrapolated boundary condition was employed, with extrapolation distance of 0.71 mfp (i.e., we assumed there was no refractive index mismatch at the boundary [21]). Twenty sources were placed at the boundary of the breast [Fig. 3(a)] and 20 detector readings were obtained for each source [Fig. 3(b)], for all reference and pathology-containing media. Both sources and detectors were positioned on the physical boundary, i.e., 0.71 mfp within the extrapolated boundary. The normalized photon intensity in

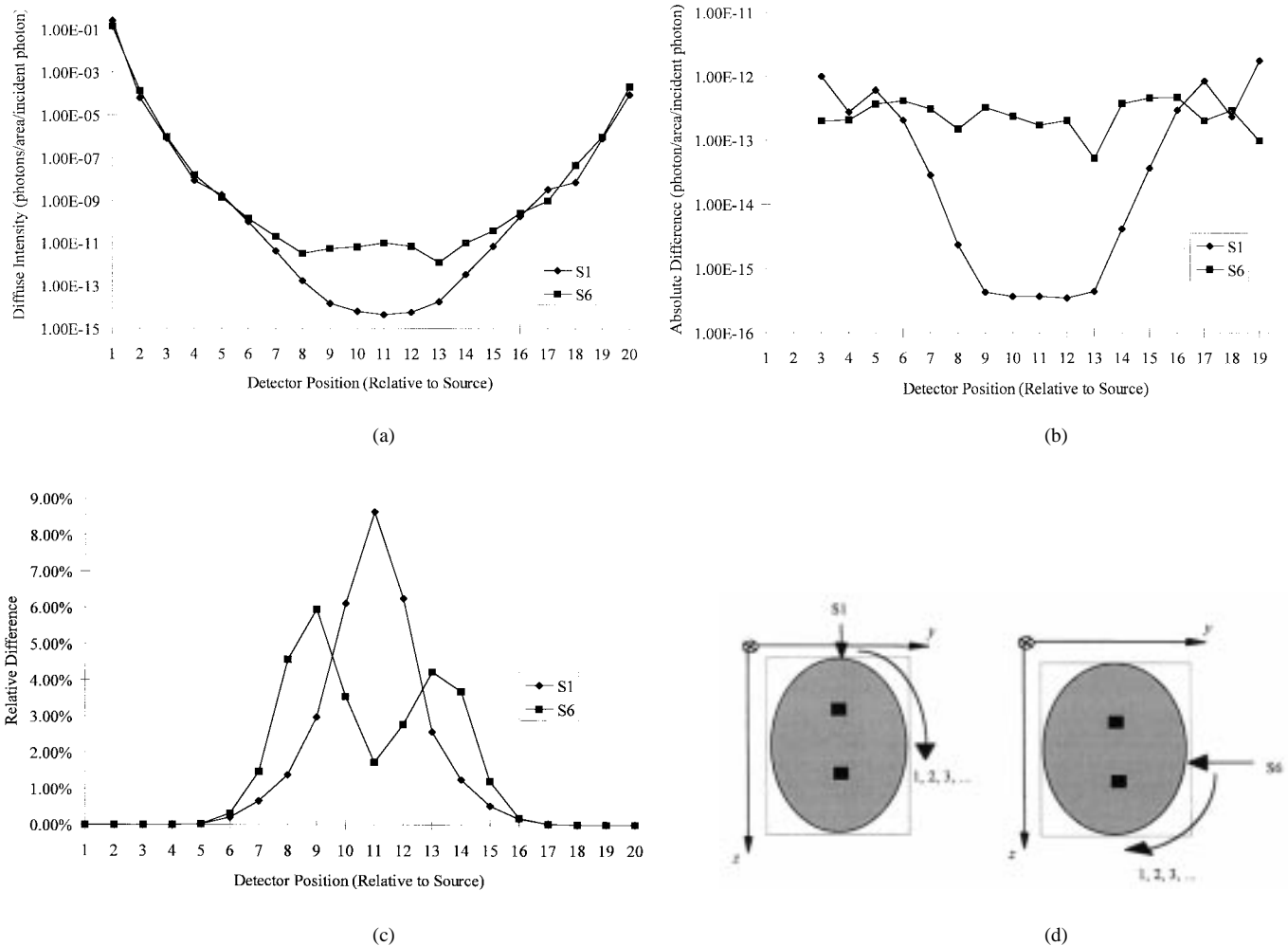


Fig. 4. (a) Reference detector readings (R_0) computed by the relaxation method, with the source at 0° (S1) or 90° (S6), for the phantom constructed from the MR breast image. (b) Absolute difference readings ($\Delta R = R_0 - R$) for the same medium as in (a). The target medium differs from the reference by the introduction of two pathologies in the upper and lower portions of the phantom. (c) Relative detector readings ($\Delta R/R_0 = 1 - R/R_0$) for the same medium as in (a). (d) Sketch indicating the source locations used for generating the two curves plotted in (a) and (c).

each voxel of the reference medium was also recorded for the weight matrix calculations.

Conjugate gradient descent (CGD) [25], with positivity constraints imposed after each iteration, was the image reconstruction algorithm used. A rescaling technique [26], which makes the weight matrix \mathbf{W} more uniform and better conditioned by setting the maximum value of each column to one, i.e., $w'_{ij} = w_{ij} / \max_{i=1}^I \{w_{ij}\}$ and rescaling every other element in proportion, was used to suppress numerical errors and accelerate convergence. Because of limitations on available computing resources, two-dimensional (2-D) reconstructions were performed by imposing translational invariance on the image in the direction perpendicular to the plane defined by the sources and detectors. That is, those voxels along a x -axis column in the breast phantom were combined by assuming $\Delta\mu_a$ was constant throughout each column, and their corresponding weights were summed up to yield a new weight function for the "combined voxels." In addition, the weight matrix size was reduced four-fold by computing a 2×2 spatial average of neighboring voxels. In all cases computed images obtained were from underdetermined data sets. Computed

images of the breast phantom contained 1584 unknowns and used 400 source-detector pairs.

IV. RESULTS

Fig. 4 shows the reference detector readings [R_0 , Fig. 4(a)], absolute [$\Delta R = R_0 - R$, Fig. 4(b)], and relative changes [$\Delta R/R_0$, Fig. 4(c)] in detector readings for the target medium caused by the added pathologies. The relative intensity difference curve [Fig. 4(c)] for source "S1" has one peak at the detectors opposite the source, while the relative intensity difference curve for source "S6" has two peaks of unequal height, and a minimum for detectors opposite the source. Fig. 5 shows forward calculation results as the logarithm of the photon intensity, along with a quantitative gray scale (photons/area), in four sagittal sections ($y = 21$, $y = 31$, $y = 35$, and $y = 41$) through the phantoms for the reference [Fig. 5(a)] and pathology-containing [Fig. 5(b)] media. Significant changes in intensity are seen at $y = 31$ and $y = 35$. Note that, as indicated in Fig. 5(c), the pathologies were actually located in the sagittal plane $y = 35$. Figs. 6 and 7 show reconstructed images of $\Delta\mu_a$, along with quantitative gray

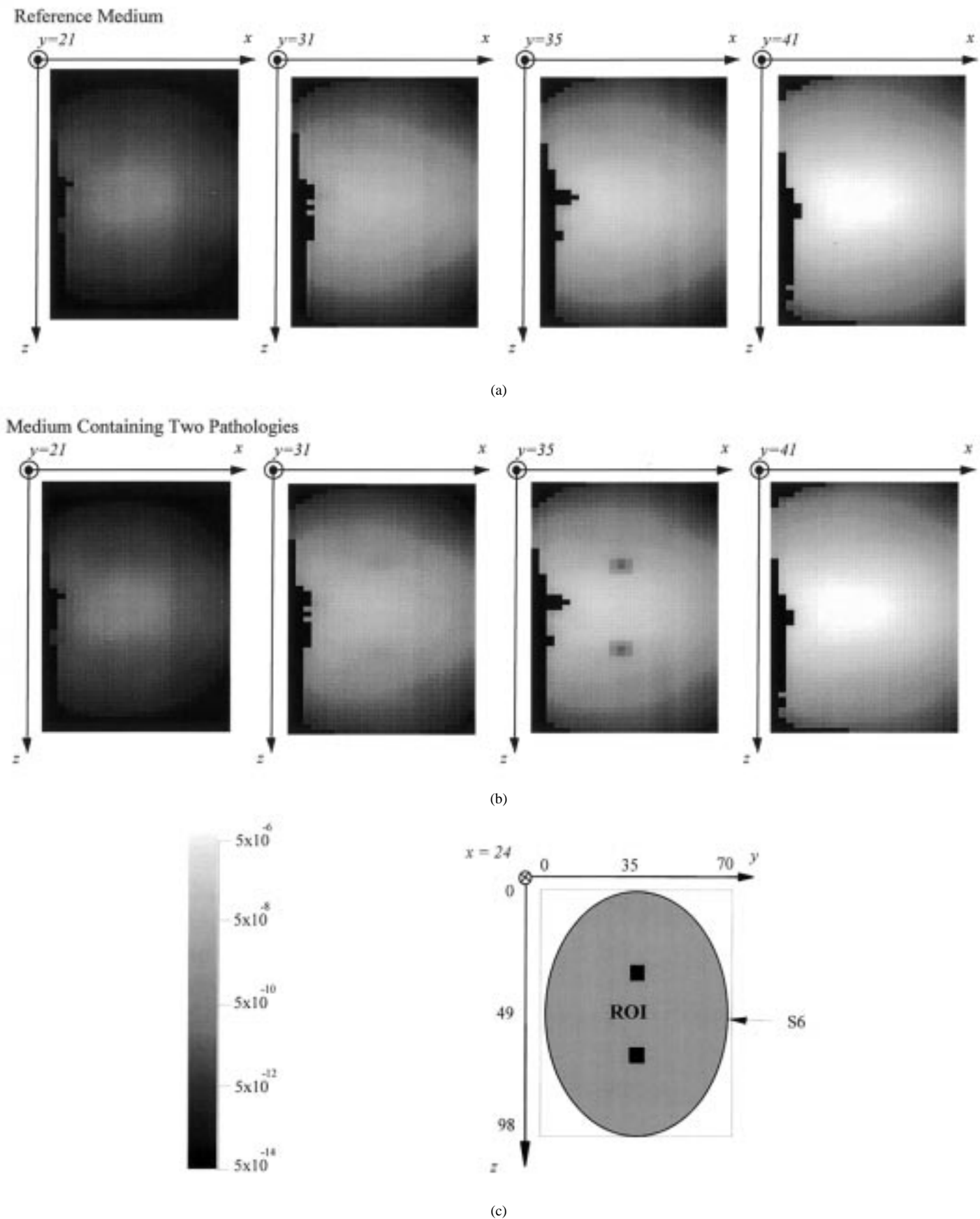


Fig. 5. Forward-problem results computed by the relaxation method for the source S6 located at (49, 69, 24), i.e., illumination from the left side of the breast. The logarithm of the photon intensity in four sagittal cuts ($y = 21$, $y = 31$, $y = 35$, and $y = 41$) is displayed for (a) reference medium and (b) medium containing two pathologies. (c) Shows a front (coronal) view, illustrating the illumination scheme. In each panel of (a) and (b), nipple is on the left side, chest wall is on the right side, and black pixels = regions outside the breast.

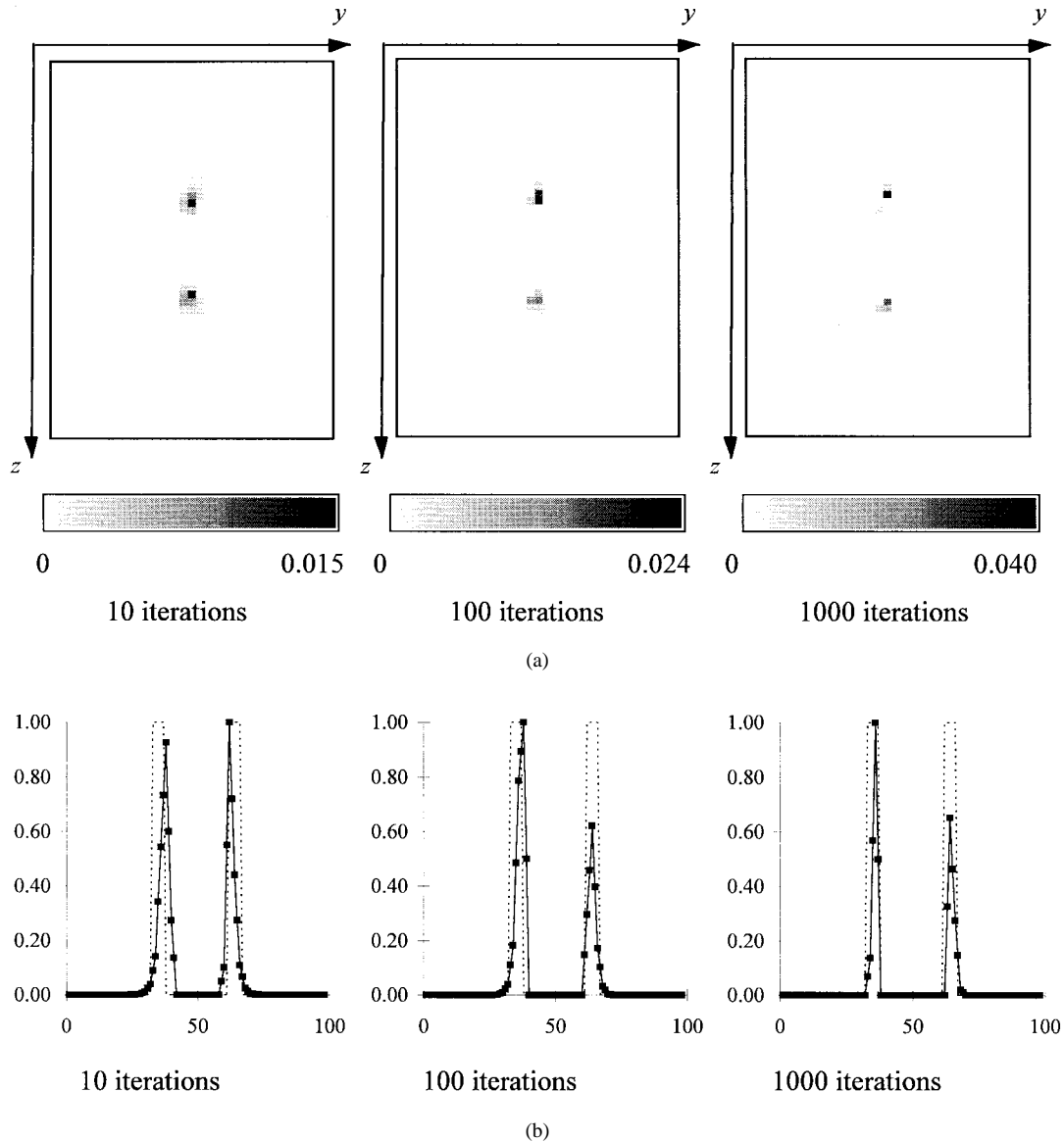


Fig. 6. (a) Reconstructed absorption cross section perturbations ($\Delta\mu_a$) using all 400 source-detector pairs illustrated in Fig. 3 and the CGD algorithm, for a two-pathology case, after 10, 100, and 1000 iterations. The weight functions were computed for a heterogeneous reference medium derived from MR images that did not include the pathologies. (b) One-dimensional profiles along the central columns where the maximum is normalized to one. The dotted lines indicate the true location and spatial extent of the pathologies.

scales (mm^{-1}), as a function of the number of iterations of the CGD algorithm, using all 400 source-detector pairs illustrated in Fig. 3. The images in Fig. 6(a) were obtained using weight functions derived from the AAO heterogeneous reference medium. Curves plotted in Fig. 6(b) are one-dimensional (1-D) profiles bisecting the images of the reconstructed pathologies seen in Fig. 6(a); the dotted lines indicate the pathologies' true locations. Fig. 7 shows the reconstructions, with quantitative gray scale (mm^{-1}), that were obtained when the weight functions were computed instead for homogeneous reference media having the same shape and volume as the AAO model, and the same μ_a and μ'_s as the AAO model's "adipose tissue."

V. DISCUSSION AND CONCLUSION

We have described an imaging method, based in transport theory, for which qualitatively accurate reconstructions are

demonstrated using media from which only multiply-scattered light can be detected. In imaging modalities such as CT, PET, or SPECT, scattered photons fundamentally constitute *noise* in the algorithms used to reconstruct the images. Considerable effort is expended, in the form of detector collimation and/or coincidence counting, to minimize the ratio of scattered to unscattered photons detected. The underlying premise is that the scattered light does not contain information about the target medium in a form that is suitable for image formation. The optical imaging method is qualitatively different, in that many-times-scattered light is the information-bearing *signal* from which the images are recovered.

The range of intensity values for detectors located on the surface of the breast phantom (Fig. 4) is very large, spanning almost 14 orders of magnitude. This exceeds the dynamic range of any physical detector, and thus attenuation of the

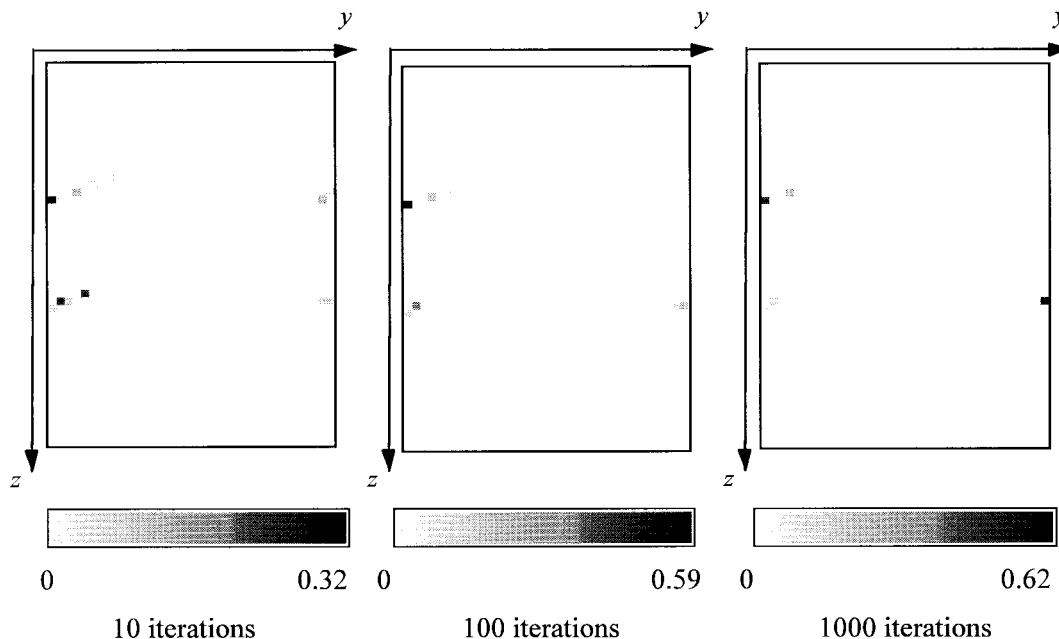


Fig. 7. Reconstructed absorption cross section perturbations ($\Delta\mu_a$) with all 400 source-detector pairs illustrated in Fig. 3 and the CGD algorithm, for a two-pathology case, after 10, 100, and 1000 iterations. In this case, the weight functions were computed for a homogeneous reference medium.

signal for detectors located near the source would be necessary in practice. Data in Fig. 4(b) shows the observed difference readings when the phantom is illuminated with the inclusions in line with and perpendicular to the source. While evidence of specific structure is difficult to determine from inspection of these data, the results in Fig. 4(c) are more revealing and suggest a pattern consistent with the added inclusions.

The forward calculation results in Fig. 5 show that significant changes in the internal photon intensity occurred in sagittal section $y = 35$, where the added inclusions were actually located. Changes were also observed in section $y = 31$, because of a shadowing effect; that is, an absorber significantly reduces the light intensity within a certain finite volume surrounding it. The reconstructed images shown in Fig. 6 clearly demonstrate that both “added pathologies” are well resolved and accurately located [Fig. 6(b)]. While these results are obtained from a heterogeneous and irregularly shaped medium, we have made use of much *a priori* information. Here the reference medium has the same geometry, internal structure (less the added inclusions), volume and optical coefficients for the background tissues as the test medium. If we employ a similar reference medium but instead assume that the background tissue is homogeneous, then, as shown in Fig. 7, only artifact is recovered. This finding is not unexpected and is certainly consistent with the known behavior and limitations of linear perturbation methods. When the reference medium is very different from the target, the linearity assumption is strongly violated and accurate images cannot be obtained from a one-step reconstruction. To obtain qualitatively good images by optical tomography using perturbation methods, one either has to have a reference medium close to the target, or

employ a multiple-step reconstruction that repeatedly updates the weight matrix and detector readings. Because the latter can require large computing costs, it would be desirable to adopt an approach from which an accurate reference state could easily be obtained.

One approach to obtaining an accurate reference state, as suggested by the modeling scheme adopted here, would be to use in practice anatomical maps as can be had from MR or CT images. This approach immediately raises the question: should such information be required, then what added benefit could be gained from performing the optical measurement? The answer to this could take many forms, but basically lies in the appreciation that optical methods are sensitive to physical properties different from those which affect the X-ray attenuation and MR phenomena. As mention in the Introduction, optical methods can be used to monitor oxygen-deficient states and changes in hemoglobin concentration. These parameters are critical to sustaining life. Beyond this, optical methods are orders of magnitude more sensitive than, for example, the MR method, especially if fluorescence measurements are made, and are well suited for monitoring dynamic events. In addition, optical instrumentation is relatively low in cost and can be made compact.

Use of CT or MR images does not, of course, provide any insight about the absorption or scattering properties of tissue *per se*. Estimates of these require independent optical measurements, as have been catalogued in other studies [27]. In practice, implementation would thus proceed by assigning estimates of the absorption and scattering cross sections to the principal tissue types identified by image segmentation methods and knowledge of the anatomy. Anatomical maps

selected for use could be obtained from an arbitrary archive, or attempts could be made to acquire the optical measurement simultaneously with the chosen imaging modality, i.e., CT or MR imaging. The latter would appear feasible especially if optical fibers are used to transmit light to and from the target tissue, because they are nonferromagnetic and therefore would not affect the magnetic field. This would confer a significant practical advantage on a simultaneous optical-MR measurement over, for example, a simultaneous PET-MR measurement [28].

The computed optical images would constitute the differences between the absorption and scattering cross sections of the defined reference state and those of the target medium. To the extent that a pathology exists and produces a large perturbation, as demonstrated here, a one-step reconstruction should be sufficient to qualitatively locate the pathology. If multiple reconstructions are performed by iteratively updating the weight matrix based on the previously reconstructed cross sections, an absolute quantitative map could be obtained, which may provide valuable additional information about tissue physiology. In either case, the AAO model would provide a good starting point. Estimates of the limits of detectability of localized perturbations in thick dense scattering media having optical properties similar to tissue [29] and studies demonstrating the sorts of errors that can result from a poor choice of reference medium [30] have been described elsewhere.

Reconstruction algorithms used here applied range constraints to confine the reconstruction to a smaller solution set. This guarantees that the reconstructed results are not too far from the real solution, especially when the system is underdetermined or ill conditioned. Moreover, the range constraints seem to have the advantage of suppressing artifact levels in the reconstructed images. The applicability of range constraints, however, strongly depends on knowledge of the target medium. In this study we imposed range constraints on the reconstruction results based on *a priori* knowledge that the absorption cross section perturbations were positive. This might also be the case in practice if, for example, we were to target a specific type of pathology whose physical properties were known to deviate in only one direction from those of the surrounding healthy tissues. On the other hand, if we were to attempt to reconstruct absolute cross sections from the AAO model with multiple updates, positivity constraints could not be applied because both positive and negative perturbations would be expected.

In conclusion, these studies directly demonstrate that in the limiting case of multiply-scattered photons, sufficient information exists at the boundary to permit accurate reconstruction of a dense scattering medium when it is evaluated using a linear perturbation model. Evidence of qualitatively good reconstructions with a single-step solution of the perturbation model suggests that the basic modeling scheme is accurate and robust. Iterative updating may be needed to obtain quantitative accuracy in the image. Future studies will involve continued examination of complex media and reconstructions obtained using time-resolved and time-harmonic illumination schemes.

REFERENCES

- [1] W.-F. Cheong, S. A. Prahl, and A. J. Welch, "A review of the optical properties of biological tissues," *IEEE J. Quantum Electron.*, vol. 26, pp. 2166–2185, 1990.
- [2] B. Chance, "Optical method," *Annu. Rev. Biophys., Biophysical Chem.*, vol. 20, pp. 1–28, 1991.
- [3] S. Feng and F.-A. Zeng, "Perturbation theory of photon migration in the presence of a single defect," in *OSA Proc. Advances in Optical Imaging and Photon Migration*, vol. 21. Orlando, FL, Mar. 1994, pp. 217–228.
- [4] K. D. Paulsen and H. Jiang, "Spatially varying optical property reconstruction using a finite element diffusion equation approximation," *Med. Phys.*, vol. 22, no. 6, pp. 691–701, 1995.
- [5] M. A. O'Leary, D. A. Boas, B. Chance, and A. G. Yodh, "Simultaneous scattering and absorption images of heterogeneous media using diffusive wave within the Rytov approximation," in *Proc. Optical Tomography, Photon Migration, and Spectroscopy of Tissue and Model Media: Theory, Human Studies, and Instrumentation*, vol. SPIE-2389. San Jose, CA, Feb. 1995, pp. 320–327.
- [6] S. R. Arridge, "The forward and inverse problems in time resolved infrared imaging," in *Medical Optical Tomography: Functional Imaging and Monitoring SPIE*, Bellingham, WA, 1993, vol. IS11, pp. 35–64.
- [7] J. Chang, H. Graber, R. L. Barbour, and R. Aronson, "Recovery of optical cross section perturbations in dense scattering media using transport theory based imaging operators and steady-state simulated data and laser measurements," *Appl. Optics*, vol. 35, pp. 3963–3978, 1996.
- [8] H. L. Graber, J. Chang, R. Aronson, and R. L. Barbour "Perturbation model for imaging in dense scattering media: Derivation and evaluation of imaging operators," *Medical Optical Tomography: Functional Imaging and Monitoring SPIE*, Bellingham, WA, 1993, vol. IS11, pp. 121–143.
- [9] Y. M. Wang and W. C. Chew, "An iterative solution of the two-dimensional electromagnetic inverse scattering problem," *Int. J. Imag. Syst., Technol.*, vol. 1, pp. 100–108, 1989.
- [10] W. C. Chew and Y. M. Wang, "Reconstruction of two-dimensional permittivity distribution using the distorted Born iterative method," *IEEE Trans. Med. Imag.*, vol. 9, pp. 218–225, 1990.
- [11] S. Oparil *et al.*, *Strategies for Managing the Breast Cancer Research Program: A Report to the U.S. Army Medical Research and Development Command*. Washington, DC: National Academy, 1993.
- [12] G. C. Tang, A. Pradhan, W. Sha, J. Chen, C. H. Liu, S. J. Wahl, and R. R. Alfano, "Pulsed and cw laser fluorescence spectra from cancerous, normal, and chemically treated normal human breast and lung tissues," *Appl. Optics*, vol. 28, pp. 2337–2342, 1989.
- [13] G. Gindi, M. Lee, A. Rangarajan, and I. G. Zubal, "Bayesian reconstruction of functional images using anatomical information as priors," *IEEE Trans. Med. Imag.*, vol. 12, pp. 670–680, 1993.
- [14] R. Leahy and X. Yan, "Incorporation of anatomical MR data for improved functional imaging with PET," in *Information Processing in Medical Imaging*. New York: Springer-Verlag, 1991, pp. 105–120.
- [15] J. Chang, H. L. Graber, P. C. Koo, R. Aronson, S.-L. S. Barbour, and R. L. Barbour, "Progress toward optical mammography: Imaging in dense scattering media using time-independent optical sources," presented at *IEEE Medical Imaging Conf.*, Norfolk, VA, Nov. 1994.
- [16] R. L. Barbour, J. Chang, H. L. Graber, P. C. Koo, R. Aronson, and S. S. Barbour, "MR assisted mammography," presented at Univ. of Penn. Conf. Integration of Medical Optical Imaging and Spectroscopy (MOI/MOIS) and Magnetic Resonance Imaging (MRI), Philadelphia, PA, Dec. 1994.
- [17] K. M. Case and P. F. Zweifel, *Linear Transport Theory*. Reading, MA: Addison-Wesley, 1967.
- [18] H. C. van de Hulst, *Multiple Light Scattering*, New York: Academic, 1980, ch. 3.
- [19] J. Fishkin, E. Gratton, M. J. vandeVen, and W. W. Mantulin, "Diffusion of intensity modulated near-infrared light in turbid media," in *Proc. Time-Resolved Spectroscopy and Imaging of Tissues*, vol. SPIE-1431. Los Angeles, CA, Jan. 1991, pp. 122–135.
- [20] A. Ishimaru, *Wave Propagation and Scattering in Random Media*. New York: Academic, 1978.
- [21] R. Aronson, "Boundary conditions for diffusion of light," *J. Opt. Soc. Amer. A*, vol. 12, pp. 2532–2539, Nov. 1995.
- [22] Y. Yao, Y. Wang, Y. Pei, W. Zhu, J. Hu, and R. L. Barbour, "Frequency domain optical tomography in human tissue," in *Proc. Experimental and Numerical Methods for Solving Ill-Posed Inverse Problems: Medical and Nonmedical Applications*, vol. SPIE-2570. San Diego, CA, July 1995, pp. 254–266.
- [23] K. A. Kang, B. Chance, S. Zhao, S. Srinivasan, E. Patterson, and R. Troupin, "Breast tumor characterization using near-infra-red spec-

- troscopy,” in *Proc. Photon Migration and Imaging in Random Media and Tissues*, vol. SPIE-1888. Los Angeles, CA, Jan. 1993, pp. 487–499.
- [24] P. C. Koo, F. H. Schlereth, R. L. Barbour, and H. L. Graber, “Efficient numerical method for quantifying photon distributions in the interior of thick scattering media,” in *OSA Proc. Advances in Optical Imaging and Photon Migration*, 1994, vol. 21, pp. 187–192.
- [25] P. E. Gill, W. Murray, and M. H. Wright, *Practical Optimization*. New York: Academic, 1981.
- [26] J. Chang, H. L. Graber, and R. L. Barbour, “Image reconstruction of dense scattering media from CW sources using constrained CGD and a matrix rescaling technique,” in *Proc. Optical Tomography, Photon Migration, and Spectroscopy of Tissue and Model Media: Theory, Human Studies, and Instrumentation*, vol. SPIE-2389. San Jose, CA, Feb. 1995, pp. 448–464.
- [27] F. A. Duck, *Physical Properties of Tissue*. San Diego, CA: Academic, 1990.
- [28] B. E. Hammer and N. L. Christensen, “Detection of positron annihilation in strong magnetic fields: The foundation for developing an MR-PET scanner,” presented at IEEE Medical Imaging Conf., Norfolk, VA, Nov. 1994.
- [29] Y. Yao, R. L. Barbour, Y. Wang, H. L. Graber, and J. Chang, “Sensitivity studies for imaging a spherical object embedded in a spherically symmetric, two-layer turbid medium with photon-density waves,” *Appl. Optics*, vol. 35, pp. 735–751, 1996.
- [30] S. R. Arridge and M. Schweiger, “Sensitivity to prior knowledge in optical tomographic reconstruction,” in *Proc. Optical Tomography, Photon Migration, and Spectroscopy of Tissue and Model Media: Theory, Human Studies, and Instrumentation*, vol. SPIE-2389. San Jose, CA, Feb. 1995, pp. 378–388.